# Wall-shear-stress measurements at moderate Re-numbers with single pixel resolution using long distance µ-PIV – an accuracy assessment

C.J. Kähler[1], R. McKenna[2], U. Scholz[1]

**Abstract** A large-format, digital, long-distance micro Particle Image Velocimetry system (µ-PIV) has been applied, to measure the wall-shear-stress and the logarithmic region of a canonical boundary layer flow along a flat plate, non-intrusively with high accuracy and spatial resolution. The fundamental aim was the accurate determination of the two *universal* constants $\kappa$ and $B$ of the logarithmic law-of-the-wall for different Reynolds numbers. This is of fundamental interest in order to provide experimental evidence that $\kappa$ and $B$ are *not* universal constants. To achieve the required measurement accuracy and spatial resolution all experimental limitations associated with the seeding, light-sheet, out-of-focus particles, optical aberrations and distortions and the spatial correlation image analysis were successfully solved. In addition, it is shown that systematic measurement errors caused by the strong illumination of the tracer particles (radiative and thermal effects) can be neglected.

## 1
## Introduction

Recently, there has been renewed interest in the turbulent boundary layer velocity profile, in particular the *universal* logarithmic law-of-the-wall after von Kármán (1930).

$$u^+ = \frac{1}{\kappa} \ln y^+ + B \qquad (1)$$

This has been partly spurred by Barenblatt's (1993) derivation of a power law for this region, which is equally grounded on dimensional analysis within the inner layer.

$$u^+ = C\left(y^+\right)^n \qquad (2)$$

The difference between the two laws is vital, however: the former neglects the effect of the molecular viscosity inside the logarithmic region of the mean velocity profile $U(y)$; the latter maintains the dependence thereon, but in an asymptotic relation. Therefore, in the limit of an infinite Reynolds number, the two are the same. When the molecular stresses $\tau_{\mathrm{mol}}$ are completely neglected relative to the turbulent stresses $\tau_{\mathrm{turb}}$, equation (1) can also be derived from the Reynolds equation, in boundary layer approximation for an incompressible 2D flow along a smooth flat plate without pressure gradient (canonical boundary layer). Due to the fact that the boundary layer approximation is only valid for infinite Reynolds number, a velocity-dependant effect is expected from a theoretical point of view. However, a unique and convincing experimental decision could not be drawn from the existing data published over the past 80 years, see figure 1. For the past decade, experimental work has therefore been focussed on measurements of turbulent velocity profiles in boundary layers, channels, pipes and ducts over a large range of Reynolds numbers using sophisticated measurement equipment (see Fernholz and Finley (1996) for boundary layer, Zanoun et al. (2003) for channel and Zagarola and Smith (1997) for pipe flows, for instance). The main findings seem to indicate a Reynolds number dependence of the velocity profiles without a pressure difference (boundary layers), with the classical theory holding where a pressure difference exists (i.e. pipes, channels, ducts). However, due to experimental reasons, the unity is still weak with regard to the suitability of each respective law. One difficulty is associated with the determination of the local wall-shear-stress $\tau_w = \mu \partial U/\partial y \big|_w$ ; with $\mu = \nu\rho$ the

1. Institute of Fluid Mechanics, Technical University at Braunschweig, Braunschweig, Germany
2. Department of Mechanical Engineering, University of Bath, Claverton Down, BA2 7JY, United Kingdom

Correspondence to:
Christian J. Kähler, Institut für Strömungsmechanik, Technische Universität Braunschweig, Bienroder Weg 3, 38106 Braunschweig, Germany
E-mail: c.kaehler@tu-bs.de

molecular viscosity of the fluid and $\partial U/\partial y$ the wall normal gradient of the mean stream-wise velocity component. This quantity is required to transform the mean velocity profile $U(y)$ into the wall-units $u^+ = U / u_\tau$ and $y^+ = y\, u_\tau / v$ respectively, by means of the friction velocity defined as $u_\tau = (\tau_w / \rho)^{1/2}$. The determination of $\tau_w$ by using well established measurement techniques such as Preston tubes, balances or hot film anemometers is – even under ideal conditions – only possible with a measurement uncertainty of approximately 5% (see Winter (1977) for details). As this is not sufficient, optical techniques can be applied such as oil-film interferometry, but the best method is the direct estimation of this quantity from the slope of the velocity profile in the viscous sub-layer where $\tau_w = const$ and $u^+ = y^+$ holds. In air this is very difficult to achieve because of the extremely thin viscous sub-layer and the very low flow velocities close to the wall. However, by using LDA or L2F this is possible in principle but, due to the restricted optical access, the darkening of the model and the size of the measurement volume, a reliable estimation is still a challenging task. Due to these inherent difficulties the method suggested by Clauser (1954) is usually applied for incompressible flows to estimate $u_\tau$. In this case equation (1) is transformed in equation (3) so that $U(y) / U_\infty$ as a function of $yU_\infty / v$ can be expressed in terms of the parameter $u_\tau U_\infty = (c_f / 2)^{1/2}$. In this representation the skin-friction coefficient $c_f$ can be obtained by matching, provided the von Kármán constant $\kappa$ and the constant $B$ of the logarithmic law-of-the-wall are precisely known.

$$\frac{U}{U_\infty} = \frac{1}{\kappa}\sqrt{\frac{c_f}{2}}\ln\left(\frac{yU_\infty}{v}\sqrt{\frac{c_f}{2}}\right) + B\sqrt{\frac{c_f}{2}} \qquad (3)$$

Unfortunately, this approach fails for the present investigation due to the uncertainty of the constants $\kappa$ and $B$ according to figure 1 and their expected dependency on the Reynolds number.
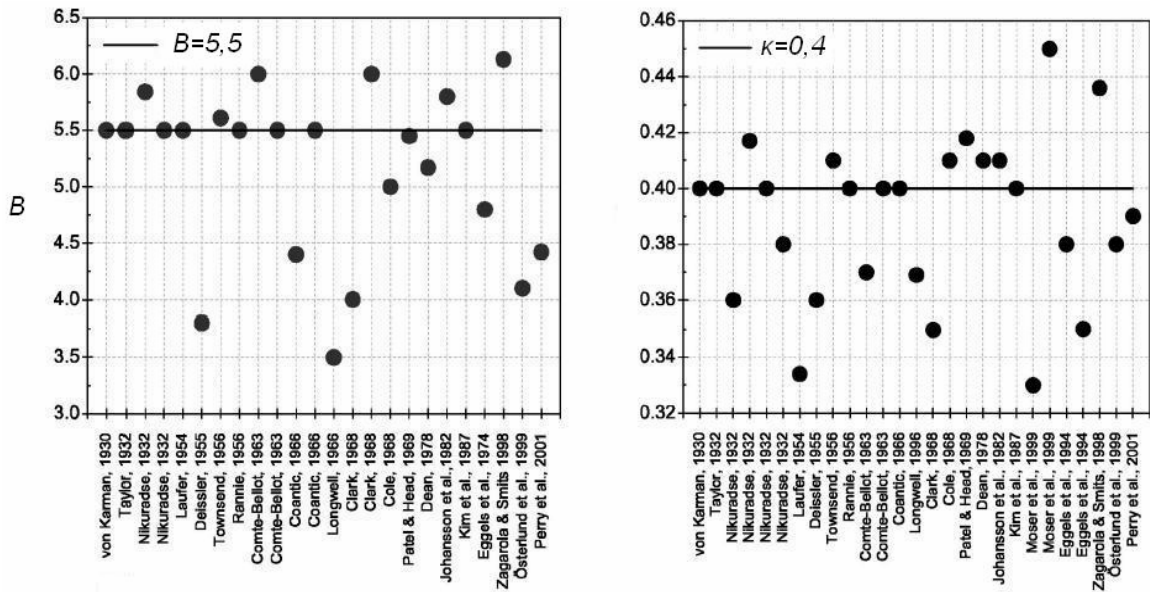


**Fig. 1**: Offset (left) and gradient (right) of the normalised mean velocity profile within the logarithmic region measured in wall bounded flows since 1930, after Zanoun et al. (2003)

To overcome the experimental difficulties, a long distance µ-PIV experiment was designed to determine the mean velocity profile of a canonical boundary layer flow along a flat plate in a low turbulence wind-tunnel at different Reynolds numbers. For the determination of $\tau_w$, the spatial resolution and measurement precision was increased by using the two-point ensemble correlation evaluation approach. On the other hand, the logarithmic region of the boundary layer flow was analysed using spatial correlation techniques because of the turbulent nature of the flow in this region. To ensure that the results are not biased due to the increased size of the measurement volume, additional experiments were performed to estimate the effect of the spatial resolution on the mean velocity profile. Finally, the root-mean-square (RMS) profile of the stream-wise and wall-normal velocity fluctuation was measured, to answer the question whether the maximum of $u^+_{rms}$ at $y^+ \approx 15$ is below the value of three (as usually measured), or above this number (as sometimes estimated from direct numerical simulations).

**2**
**Methodology**
μ-PIV has recently developed from the PIV technique, whereby an instantaneous fluid flow field is obtained by statistically correlating images of tracer particles in the flow. The main differences of large-format, digital, long-distance μ-PIV to conventional PIV are the large tracer-particle concentration required to sample the flow, the out-of-focus effects due to the thin depth-of-focus and the effects of image aberrations and distortions by the imaging device. These issues will be illuminated in more detail in the following subsections.
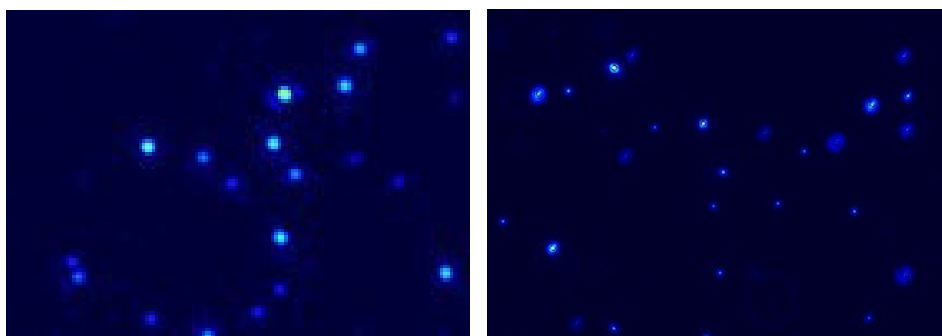
**Imaging characteristic**
First of all, it is very important for accurate PIV measurements that the particle images are nearly circular with a good natured intensity distribution (no holes). Therefore, the starting point of the experimental investigation was a performance test between two different optical microscope concepts. The market leaders are the *Questar QM-1* reflecting and the *Infinity K2* refracting microscope (see reference for details). Of primary interest was: firstly, the quality of the particle images, secondly, the magnitude and direction of optical aberrations and, thirdly, the effect caused by the shadowing. The latter effect is typical for near-wall boundary layer experiments because only the upper half of the microscope can be used for the accumulation of the light scattered by the particles as the lower half is blocked by the flat plate. This aperture effect results in optical aberrations as shown in figure 2.
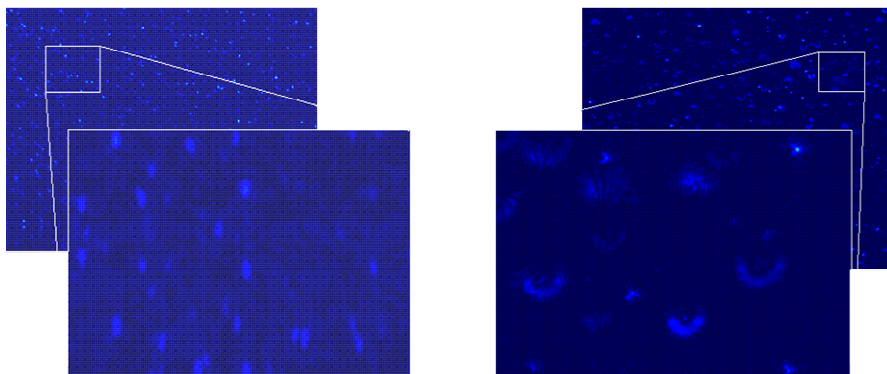


**Fig. 2**: Performance test between the refracting Infinity K2 (left) and the reflecting Questar QM-1 microscope

In the case of the Infinity K2 microscope (left image) it can be seen that the shadowing promotes astigmatism, with the main stretching of the particle images in the direction normal to the model surface. Nevertheless, the intensity distribution and the contour of the particle images are quite good and, without the darkening of the model, completely circular (see left image of figure 3). The Questar QM-1, in contrast, reveals larger particle images with an undesired intensity distribution and shape. Without the model in front of the lens the performance of both devices is comparable (figure 3) and the Questar QM-1 is as well applicable for μ-PIV investigations, as demonstrated by Dieterle (1997) and Lindken et al. (2002). However, for the present investigation only the K2 could be applied.



**Fig. 3**: Particle images recorded with the Infinity K2 (left) and the Questar QM-1 (right) microscope with full optical access (no darkening of the front lens). The size of both sub-images is identical.

**Distortion characteristic**

All µ-PIV applications are faced with the problem that the field of view is very small due to the high magnification factor. To overcome this drawback at least partially, a cooled CCD camera from PCO with 4008×2672 pixel resolution and 14bit dynamic range was applied for the measurements. Due to fact that the microscope is not designed for 36.6×24.5 mm$^2$ sensor dimensions, tests were performed to quantify the distortions and the loss of intensity towards the edges of the field of view. Therefore, regular grids with different line spacing (0.05 to 1.0 mm) were manufactured with a CNC milling cutter. Because equidistant grid spacing is extremely important to assess the image quality properly, the machine was equipped with a fine tube, instead of a cutter, in which a steel needle was partially interposed. By using this instrument it was possible to scribe a very fine high quality grid in acrylic glass with any appropriate line spacing. The depth of the chink was always constant because of the constant contact pressure of the needle due to the air cushion mechanism. The grids were used to detect and compensate optical distortions digitally prior to the evaluation of the images. This is important, in particular for boundary layer experiments, because the optical distortion effect is usually amplified, as only the upper half of the lens is used to collect the light. This is based on the optical effect that the shape and position of the aperture (in this case the model in front of the microscope) affects the image properties locally (as shown in figure 2) and globally (in form of distortions), see Bergmann and Schäfer (2004) for instance.

**Illumination**

Binocular µ-PIV systems are usually faced with the problem that a sheet illumination is impossible because the thickness of the light-sheet is usually large compared to the depth-of-focus of the imaging system (see Wereley et al. (1999), Meinhart et al. (2000)). As the measurement precision strongly depends on the image quality, the suppression of the background noise caused by unfocussed particles is one of the most important challenges. In case of the long distance microscope this fundamental problem is of minor importance, because at a wavelength of λ=532 nm the depth-of-focus is already around 100 µm when a magnification of 14 and a numerical aperture of 0.07 is assumed. The intensity of the light source, on the other hand, is a limiting factor in long distance µ-PIV applications due to the small aperture of the imaging system and the relatively large distance from the measurement plane. To solve these problems, the laser beam of a frequency doubled Nd:YAG laser (*Quantel Brilliant*) with 150 mJ output energy per pulse was expanded and afterwards re-focussed in the same direction by means of a pair of cylindrical lenses with $f$ = 40 mm and 200 mm focal-length. By using this optical configuration the light-sheet width at a particular position behind the oscillator is simply determined by the diameter and divergence of the laser beam. The light-sheet thickness at the focal line of the lens pair on the other hand can be around 50 µm if required (this is usually close to the lower practical limit due to the finite size of the resonator). When the distance between the light-sheet optic and the measurement domain is a few metres, the light-sheet thickness is approximately constant over the entire region of interest because the linear dimensions of the observation area are only a few millimetres. In boundary layer experiments, special care must be taken with the propagation direction of the laser relative to the model. When the propagation direction is not parallel to the model surface strong diffuse reflections may cause problems in the near-wall region. However, more serious is a local melt out of the model caused by the high energy density at the focal line, or in the worst case a generation of artificial turbulent flow structure, see Kähler and Scholz (2003) for details. As this would alter the flow under consideration in the experiments outlined here, the propagation direction of the light was always parallel to the model surface.

**Seeding**

Essentially, the large tracer-particle concentration $C$ required for µ-PIV experiments results from the large magnification factor $M$ and the thin light-sheet thickness, which in turn has to be employed because of the low aperture and depth-of-focus of the optical instrument. In order to achieve a completely homogeneous seeding concentration, as required for the bias free estimation of the flow velocity, global seeding is usually the most appropriate solution for turbulent boundary layer experiments, Kähler (2004). However, due to the huge number of particles required, this approach is not feasible for long distance µ-PIV applications, because the particles between the microscope and the measurement plane deteriorate the image contrast due to absorption and multiple particle scattering. Therefore different local seeding approaches have been tested to deposit the particles inside the desired stream-tube of the flow. The injection of the seeding was done at the entrance of the Eiffel-type wind-tunnel in front of the honeycomb and screens. This is required to avoid a change of the base flow in the test section. Commercial smoke generators based on the principle of evaporation could not successfully be applied in the experiment because the high temperature of the air / seeding mixture delivered by the generator alters the base flow in the test section due to the amplified diffusion. This could be clearly observed in preliminary tests. Also not recommended are particle generators that generate large particles. In this case a slight liquid-film caused by the settling of the particles

at the model can be detected after a while. Beside a possible modification of the boundary conditions (the position were the non-slip condition holds is slightly displaced) this results in undesired diffuse reflections at the wall and thus in an attenuation of the image quality. For these reasons seeding generators based on the atomisation of oil have been employed for the experiments, see Kähler et al. (2002) and Kähler (2003).

**Radiative force and thermal effects**

Recently it has been demonstrated that the power of a focussed PIV laser beam can alter the flow structure and the boundary conditions, Kähler and Dreyer (2004). Due to the high energy density at the focal line where the measurements take place, it cannot be precluded that undesired effects appear, which increase the measurement uncertainty or alter the turbulent boundary layer. To prove and quantify the impact of the radiative forces and thermal effects, the experiment displayed schematically in fig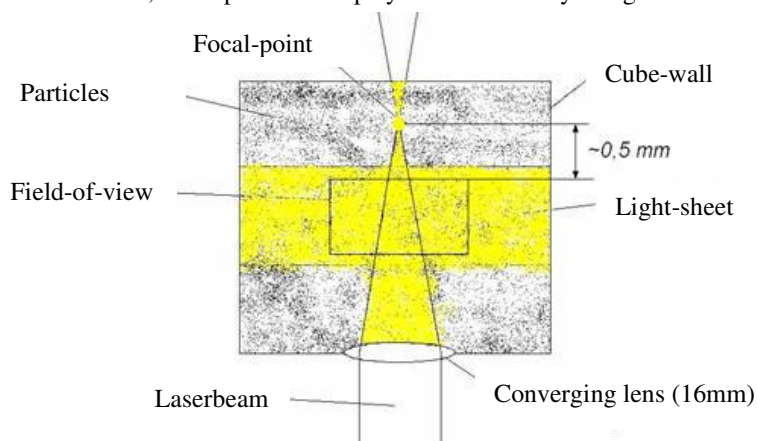ure 4 was realised. The measurements were performed in a 30mm long glass box to eliminate as far as possible any convectional flow within the fluid. A 16 mm convex lens positioned in the lower side of the box allowed a second, influencing laser to be focussed above the measurement window.

To investigate the effects on the measurement accuracy the particle laden flow was strongly disturbed by means of the focussed laser beam from below and the verification of the effect was realised by means of the μ-PIV system. As the intensity of the primary laser beam increases continually towards the focal point the effect caused by the radiative force must increase with decreasing distance from the focal point. In contrast to the pressure due to radiation, which is directional, the thermal effects are circular or isotropic but as well a function of the position inside the converging laser beam. This makes it possible to separate both effects on average. For the experiment the particle image position at rest was measured first with a single illumination from the left hand side with horizontal polarisation (the camera was equipped with a polarisation filter such that only radiation coming from the horizontal laser-beam could be recorded). Thereafter the position of the particles was affected by means of the converging laser beam from below, whereby the polarisation state of the radiation was orthogonal to the other two laser pulses. The new position of the particles was finally measured by means of the second laser pulse from the side. By varying the temporal separation between the two equally polarised laser pulses it was possible to align the measurement accuracy of the registration system and by averaging the results for each $\Delta t$ over 300 samples random errors, due to convection for instance, could be eliminated. The largest systematic displacement error in the experiment was 0.5 pixels (0.45 μm) after 20 μs. By taking into account that the pulse separation is up to 10 times smaller for the boundary layer experiment (see table 1) and the laser power only a fraction of the power generated by the focussed laser pulse, it can be concluded that the measurement accuracy of the μ-PIV system is not reduced due to the effects considered so far, provided the energy density is always below that required for the optical break-down of air, see Kähler and Dreyer (2004).

**Fig. 4**: Set-up for the investigation of radiative and thermal effects

**3**

**Two-point ensemble correlation PIV**

To increase the spatial resolution and measurement precision for the estimation of $\tau_w$ a two-point ensemble correlation evaluation approach was developed based on the work of Adrian (1988) and Westerweel et al. (2004). By using this method it is possible (at least in principle) to retrieve mean velocity information up to a resolution of a single pixel, provided the flow is *laminar* and *stationary*. The principle of the method is schematically shown on the left hand side of figure 5. For all $N$ image pairs the intensity value of the pixel at the position $i, j$ in frame 1 is correlated with the intensity value of the pixel $i+\Delta r, j+\Delta s$ in frame 2. Thereafter the ensemble average is calculated over all results and properly normalised according to equation (4) and (5) to obtain a unique peak of the correlation

coefficient as shown in the right image of figure 5. It is obvious that a well defined signal peak can only be obtained when the flow is stationary and the displacement caused by the turbulence level is below the size of the correlation peak width projected in physical space. The two-point ensemble correlation has been implemented straight forwardly, which leads to total number of *MNmn* calculations per image pair, where *M, N* are the dimensions of an image and *m, n* are the dimensions of the correlation plane. *MNmn* is also the number of variables to be held in memory. After the correlation step, the maximums are searched for.

To obtain sub-pixel accuracy, different peak-fitting routines were implemented based on a least squares fit of Gaussian shape functions. The typical three-point Gauss-fit is implemented, as well as a 3×3 point Gauss-fit and a *n*×*n* point Gauss-fit where the coefficients are determined by a Levenberg-Marquardt approach. In the post-processing step the velocity vectors are validated. Beside a median filter, the peak ratio (defined as the highest divided by the second highest correlation coefficient) and the peak height are taken into account for the validation. If the vector resulting from the first peak does not fulfill all criteria the second peak is tried with the two remaining validation criteria median filter and peak height.

$$c^{\Delta r,\Delta s}(i,j) = \frac{\sum_{n}^{n}\left(I_{i,j}^{n} - \overline{I_{i,j}}\right)\left(I_{i+\Delta r,\,j+\Delta s} - \overline{I_{i+\Delta r,\,j+\Delta s}}\right)}{\sigma_{i,j}\,\sigma_{i+\Delta r,\,j+\Delta s}} \qquad (4)$$

$$\sigma_{i,j} = \sqrt{\frac{1}{N-1}\sum^{N}\left(I_{i,j}^{n} - \overline{I_{i,j}}\right)^{2}} \qquad (5)$$
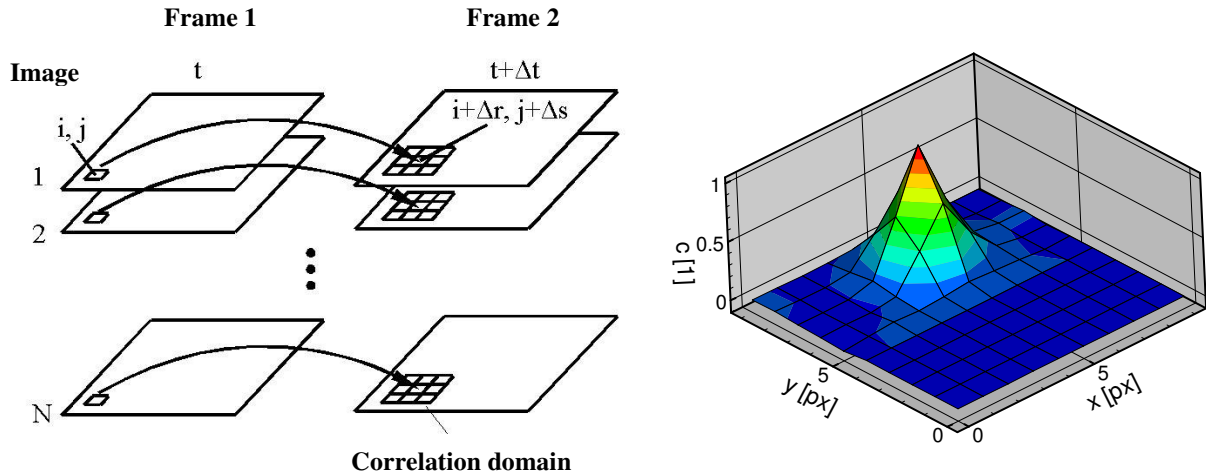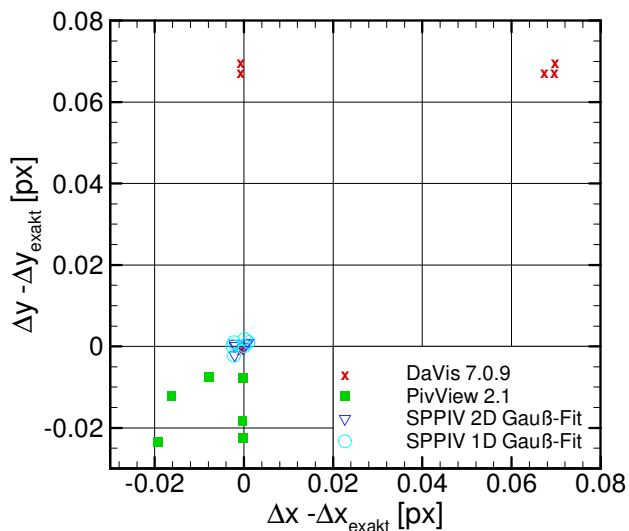


**Fig. 5**: Two-point ensemble correlation approach (left) and normalised correlation peak (right)

Many standard PIV methods have implemented initial shift und reference velocity field capabilities, to reduce the effect of in-plane loss-of-pairs. For the two-point ensemble correlation evaluation this is not needed to enhance the signal strength because the effect does not exist. But it can be used for reducing the size of the correlation plane of size *MNmn* when high particle image displacements are expected. For example a 1280×1024 px double image pair with 32×32 px correlation plane size would yield 5 GB of memory which exceeds the present maximum memory size of around 4GB (32bit addressing). For handling such memory requirements a block-wise evaluation was implemented, where the images are split into several blocks and the blocks are evaluated in sequence. This block structure simplifies the possibility of a parallelisation in order to further decrease the evaluation time. To avoid a loss of time caused by computer crashes and program interruptions a restart-functionality was implemented in addition.

**4**

**Validation of the two-point ensemble correlation algorithm**

To validate the two-point ensemble correlation algorithm several test cases have been investigated. Three of them are based on synthetic PIV images created with a home made high-performance image generator, which in turn was validated by using the synthetic image generator S.I.G., developed within the EU project Europiv II, and the particle image generator SIMPIV, developed at the German Aerospace Center (DLR) in Göttingen. The first test case is a uniform flow field, the second a laminar flow and the third a laminar flow with superimposed normal distributed turbulence (or noise) level. In addition, the effect of particle image diameters on the measurement error is investigated. In the first case, the precision of the developed method is compared with two commercial PIV evaluation packages (DaVis 7.0.9 from LaVision and PivView 2.1 from PIVTEC) for different displacements in $x$ and $y$ directions. The exact particle image displacement is 1.0, 0.5 and 0.25 px in each direction. With these displacements a test matrix of all combinations was evaluated. For the two-point ensemble correlation method a 130×130 px image was used with a particle image density of 20 particle images per 32×32 px. The total number of double images was 2048. For the commercial PIV packages DaVis 7.0.9 and PivView 2.1 a 2048×2048 px double image was applied. Further parameters for the synthetic PIV image generator were a particle image diameter d of 2.0 with no fluctuations of the size, a top-hat beam profile, a camera dynamic of 8bit and no noise.



**Fig. 6**: Measurement error of the two-point ensemble correlation (SPPIV) compared to conventional programs from LaVision (DaVis) and PIVTEC (PivView)

The result of the comparison is displayed in figure 6, where the differences of the calculated displacement components $\Delta x$, $\Delta y$ relative to the exact values $\Delta x_{exact}$, $\Delta y_{exact}$ are shown. It can be stated that the differences are all below 0.08 px. For 1.0 px displacement the commercial packages differ from the exact solution by <0.001 px, whereas the two-point ensemble correlation (SPPIV) reaches values <0.0001 px. For the other displacements the absolute errors are higher, but for the two-point ensemble correlation method the errors are always the smallest (<0.002 px). This result implies the potential gain in accuracy that can be obtained for the determination of $\tau_w$. However, it should also be emphasised that this is a synthetic test case. For realistic test cases the performance is usually reduced by an order of magnitude, but even then the accuracy of the two-point correlation is remarkable, especially when the spatial resolution is taken into account.

Only for a few PIV applications can a flow be assumed to be laminar and stationary. Billy et al. (2004) have already applied the two-point ensemble correlation approach to a time dependent laminar flow, but in fluid mechanics turbulent flows are usually of primary interest. To study the influence of turbulence, synthetic particle image fields were created and evaluated with different peak-fitting methods. The artificial turbulence is simulated by adding normally distributed random values with a standard variation of 1 px to the displacement. The displacement field has been chosen to be uniform with a shift of 2 px in the $x$-direction. Further parameters are a particle image diameter of 2 px, a particle image density of 20 particle images per 32×32 px and no noise. For the evaluation 4000 double images with 256×256 px resolution were used, which leads to a statistic base of 65536 velocity vectors. Figure 7 implies that the main effect is the broadening of the correlation peak due to the turbulence. It is obvious that the broader the peak is the more difficult is the peak-fitting. Therefore it can be expected that a peak-fitting method based on a higher number of correlation plane values will be superior to a method with fewer values. In figure 7 (left) the probability density function of a laminar flow with 2 px displacement in $x$-direction is shown. The RMS of the distribution is around 0.05 px. Because of the ideal conditions the correlation coefficient is very high (>0.9) and the correlation peak is small. Therefore the higher peak fitting methods do not have an advantage compared to the 3 point Gauss-fit but cost more computational effort. Adding the simulated turbulence spreads the probability density function significantly, as shown in figure 7 (right). In that case the accuracy of the peak fitting can be increased by taking more correlation plane values around the peak into account. In the right graph the RMS of the distribution decreases from ~0.129 for the 3 point Gauss-fit to ~0.091 for the 11×11 Gauss-fit.

It is important to accent that the position of the maximum matches nicely with the average value of the displacement. Thus it is possible to apply this correlation method also for weak and strongly turbulent flows. However, in the latter case the distribution of the fluctuations must be symmetrical in order to avoid bias errors. Unfortunately this is not the case for the flat plate boundary layer flow in the buffer-layer and the beginning of the
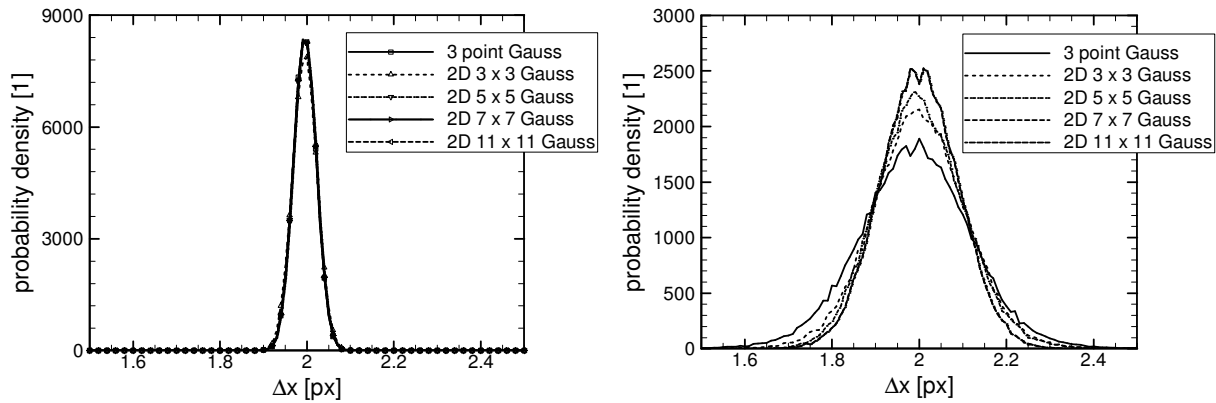


**Fig. 7**: Probability density function of a laminar flow with 2 px displacement in *x*-direction (left) and a artifical turbulent flow with $\Delta x = 2$ px mean displacement and $\Delta x_{rms} = 0.05$ px turbulence intensity (right)

log-law region, see Kähler (2004b) for instance. For this reason the conventional evaluation method based on spatial correlation has to be applied for the calculation of the mean velocity profile at $y > 5$.

For real long distance µ-PIV applications the particle image diameter *d* can be 30 pixel according to figure 2 and 3 due to the small numerical aperture. In case of standard PIV this leads to a broadened correlation peak and hence a decrease in accuracy for the 3 point Gauss-fit estimator according to Adrian (1997). The optimum particle image diameter is around 2 px for digital PIV. To analyse the behaviour of the two-point ensemble correlation approach 5000 synthetic PIV images with 256×1000 px resolution have been generated with a linear *y*-velocity gradient in *x*-direction. The velocity changed from –1 px to +1 px along the whole image width. The number of particles per 32×32 px area was decreased in order to have a constant area of particle images in the image ($d = 2 \rightarrow 100$ particles per 32×32 px, d = 4 → 25 particles per 32×32 px), with a minimum of 1 particle per 32×32 px. The peak detection was estimated with a 3 point Gauss estimator. Figure 8 (left) shows the difference between the calculated displacement and the exact displacement along the *y*-coordinate, which is equal to the *x*-displacement due to the
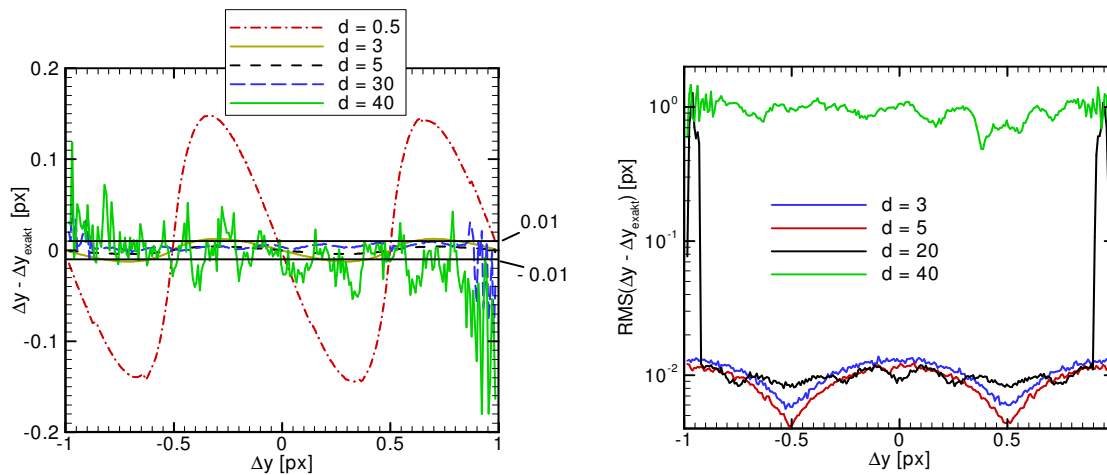


**Fig. 8**: Dependency of the measurement error $\Delta y - \Delta y_{exact}$ (left) and RMS($\Delta y - \Delta y_{exact}$) (right) from the particle image displacement $\Delta y_{exact}$ and particle image diameter d

linear displacement gradient. For particle image diameters below 1 pixel strong peak-locking effects can be observed, resulting in systematic errors of maximal 0.15 px. With increasing particle image diameter these errors

decrease to a small band of ±0.01 px. When the large particle image diameters are approached ($d = 40$), the number of particles contributing to a correlation peak decrease and therefore the measurement error increases. In tendency the ±0.01 px band is also the measurement uncertainty, when the number of images is high enough. It is also interesting to observe the behaviour of the RMS of the difference between the calculation and the exact solution. Figure 8 (right) shows that behaviour for the particle image diameters 3, 5, 20, 40. Smaller particle image diameters have been left out for clarity, because the existence of peak-locking effects is obvious from the left graph. It can be seen that the RMS is smallest at half pixel displacements. Even for large particle image diameters up to 20 this behaviour can be observed. Only for a particle image diameter of 40 pixels can this effect no longer be observed. This is due to the fact that the noise associated with the determination of the correlation peak maximum is getting very large relative to the error caused by peak-locking, because of the extremely small curvature of the peak around the maximum. For the sake of completeness it should be mentioned that the strong increase of the RMS values at the border of the image appear if the particles are not fully inside the image field, because in this case the correlation plane is biased. For the $d = 40$ px case alone this effect cannot be observed at all due to the aforementioned noise. The analysis of the results indicate clearly that the application of the two-point ensemble correlation method is advantageous for the determination of $\tau_w$ because of the higher spatial resolution and measurement accuracy, especially when the diameter of the particle image size is large, as common in digital, long-distance μ-PIV applications. However, due to the large size of the particle images it is clear that the estimation of the velocity at a single pixel incorporates the information of the surrounding fluid but with less weight due to the circular geometry of the particle images and their Gaussian intensity distribution.

## 5
### Experimental boundary layer results

The turbulent boundary layer experiment was performed in the closed test-section of the Eiffel-type low noise wind-tunnel at TU Braunschweig (LNB). The length, height and width of the fully transparent test-section is $1500 \times 600 \times 400$ mm$^3$, the contraction ratio is 15:1 and the turbulence level was measured with a hot-wire to be 0.1% for free-stream velocities > 10m/s. The 1000 mm long, 400 mm wide and 10.6 mm thick flat aluminium plate with elliptical leading edge (aspect ratio 6) was mounted horizontally in the centre of the test-section. The pressure gradient along the plate was compensated for by means of a slightly divergent orientation of the wind-tunnel walls. To fix the transition a sandpaper trip was attached to the plate. For the investigation of the velocity profiles the *Infinity K2* long distance microscope was used in conjunction with a 11 mega-pixel CCD camera (*PCO4000*). A double pulse Nd:YAG laser (*Quantel Brilliant*) was employed to generate the light-beam, which was formed into a sheet with two cylindrical lenses having focus lengths of 40 mm and 200 mm respectively. Recordings of 1000 images were made at the maximum magnification (14.3), as well as a reference measurement of 5000 images at a smaller magnification (2.2). The low magnification test case was performed in order to estimate spatial resolution effects. Seven experiments were performed at two stream-wise locations ($x = 350$ and $680$ mm) and at 4 different free stream velocities ($U_\infty = 8, 10, 12$ and $16$ m/s). The following table indicates the full test program and all relevant parameters.

| $Re_x$ | 2,4E+05 | 1,9E+05 | 2,9E+05 | 4,0E+05 | 1,9E+05 | 2,4E+05 | 3,8E+05 |
|---|---|---|---|---|---|---|---|
| $Re_\theta$ | 6,6E+02 | 6,1E+02 | 7,5E+02 | 0,0E+00 | 6,1E+02 | 6,7E+02 | 9,4E+02 |
| $Re_\delta$ | 2,4E+03 | 2,2E+03 | 2,7E+03 | 3,2E+03 | 2,2E+03 | 2,5E+03 | 3,1E+03 |
| | | | | | | | |
| $U_\infty$ (m/s) | 10 | 8 | 12 | 8 | 8 | 10 | 16 |
| $u_\tau$ (m/s) | 0,450 | 0,362 | 0,528 | 0,353 | 0,381 | 0,451 | 0,668 |
| $\delta_{98}$ (mm) | 9,23 | 9,66 | 8,80 | 14,15 | 9,66 | 9,23 | 7,95 |
| $\delta^*$ (mm) | 1,43 | 1,50 | 1,35 | 2,42 | 1,50 | 1,43 | 1,24 |
| $\theta$ (mm) | 0,97 | 1,10 | 0,91 | 1,67 | 1,10 | 0,97 | 0,85 |
| | | | | | | | |
| **Field of view x$_1$ (mm)** | 3,75 | 2,51 | 2,51 | 2,47 | 2,52 | 2,52 | 2,51 |
| **Field of view x$_2$ (mm)** | 3,00 | 1,67 | 1,67 | 1,65 | 1,68 | 1,68 | 1,67 |
| **Spatial resolution (mm$^3$)** | 0,75 x 0,05 x 0,5 | 0,32 x 0,04 x 0,5 | 0,32 x 0,04 x 0,5 | 0,32 x 0,04 x 0,5 | 0,32 x 0,04 x 0,5 | 0,32 x 0,04 x 0,5 | 0,32 x 0,04 x 0,5 |
| **Time delay (μs)** | 4 | 6 | 4 | 6 | 6 | 5 | 2 |
| **Dynamic range (pixel)** | $0,3 < \Delta x < 11,0$ | $0,3 < \Delta x < 54,3$ | $0,5 < \Delta x < 56,6$ | $1,0 < \Delta x < 54,5$ | $1,1 < \Delta x < 56,0$ | $1,2 < \Delta x < 58,4$ | $1,3 < \Delta x < 38,1$ |
| | | | | | | | |
| Vectors per sample | 1143 | 1148 | 1148 | 1148 | 1148 | 1148 | 1148 |
| Number of Samples | 5000 | 1000 | 1000 | 1000 | 1000 | 1000 | 1000 |

**Table 1**: Boundary layer and recording parameters

It is important to emphasis that some of the experiments have been performed with different settings of the camera sensor in order to validate the effect of the system components on the fluid mechanical result as well. In the following representation the subscript _2 attached to the case in the legend indicate the second run with different sensor settings (lower background and read-out noise). Figure 9 reveals all measured non-dimensional velocity profiles in semi-logarithmic representation along with the theoretical result based on equation (1) with typical values for the constants. It can be seen that the agreement in the near-wall region ($y^+ < 10$) is very good for all measurements. However, in the buffer-layer and the adjacent logarithmic region the results are grouped in two profiles with a spacing of approximately 0.8 $u^+$ units. The upper collection of graphs was measured with a very high spatial resolution and without artificially amplified background and read-out noise of the CCD camera. The lower collection on the other hand can be obtained when the spatial resolution is too crude or the signal to noise ratio is not
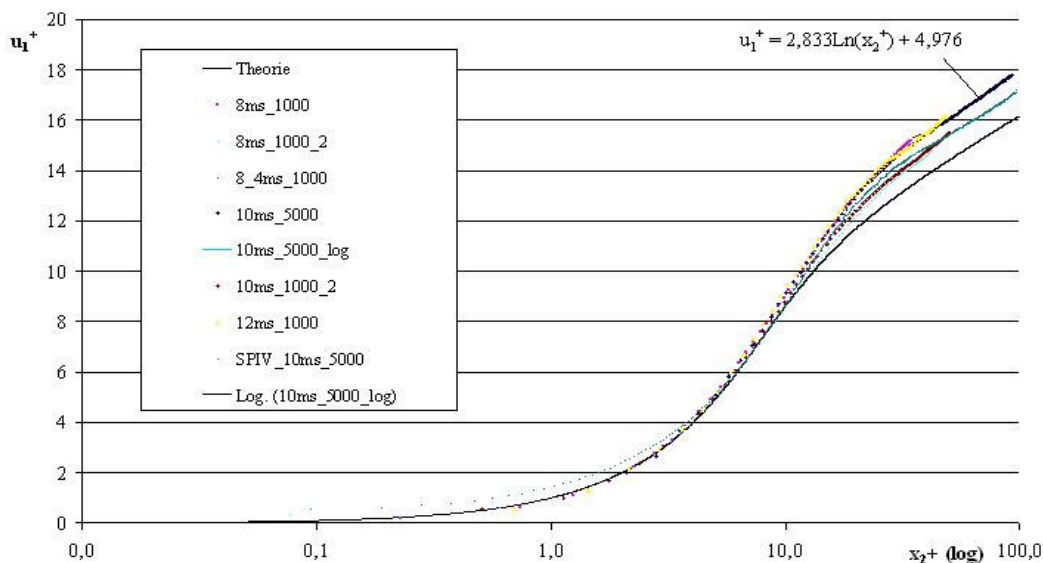


$$u_1^+ = 2,833 \, Ln(x_2^+) + 4,976$$

Legend:
- Theorie
- 8ms_1000
- 8ms_1000_2
- 8_4ms_1000
- 10ms_5000
- 10ms_5000_log
- 10ms_1000_2
- 12ms_1000
- SPIV_10ms_5000
- Log. (10ms_5000_log)

**Fig. 9**: Semi-logarithmic representation of the mean velocity profile in wall-units



Legend:
- u1+_2nd_8ms
- u2+_2nd_8ms
- u1+'_10ms_5000_1
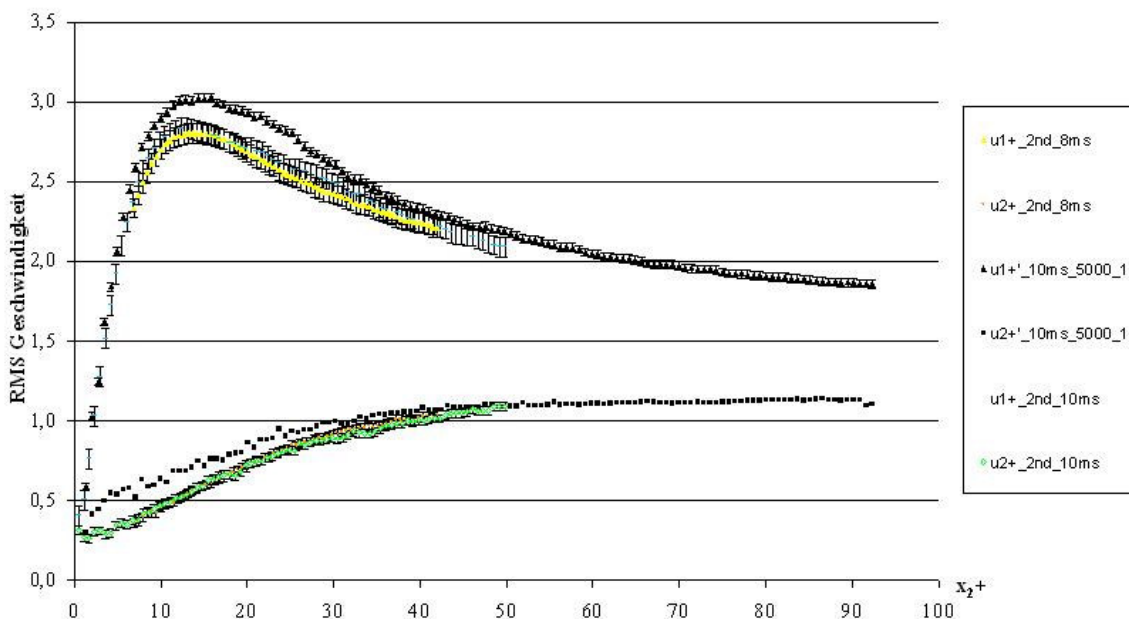- u2+'_10ms_5000_1
- u1+_2nd_10ms
- u2+_2nd_10ms

**Fig.10**: Linear representation of the stream-wise and wall-normal velocity fluctuations (RMS) in wall-units

fully optimised. This implies clearly the significance of the system quality and its proper alignment. With respect to the two constants the analysis of the results yields $\kappa = 0.35$ and $B = 4.98$ for the log-law fitting, which is close to the recently determined $\kappa = 0.35$ by Österlund et al. (2000). The power-law fitted to the reference measurement yields $C = 8.37$ and $n = 0.17$. Figure 10 shows the dependence of the stream-wise and wall-normal velocity fluctuations (RMS) in wall-units. It can be seen that a low spatial resolution (test cases with 5000 samples) results in an increased RMS value, in particular in the domain with large fluctuations ($y^+ < 40$) and strong gradients of the mean velocity. The other results, on the other hand, are quite close together (the results with the modified CCD sensor characteristic are not shown in this graph). In addition, it should be noted that the maximum of the mean stream-wise velocity fluctuation is around 2.8, in accordance with the results collected by Fernholz and Finley (1996) and Kähler (2004) for instance, and not above 3.0.

## 6
## Conclusions

1. The comparison of the two microscopes, the Questar QM-1 and the Infinity K2 indicate that the latter one is better suited for long-distance μ-PIV investigations in boundary layers because of weaker aperture and shadowing effects (Fig. 2 and 3).
2. When the image acquisition is performed with large format CCD cameras the image distortions need to be compensated digitally prior to the evaluation.
3. For long distance μ-PIV boundary layer measurements the propagation direction of the light sheet should be parallel to the model to avoid strong diffuse wall reflections and a distortion of the model surface and the flow properties.
4. Due to the high tracer particle concentration required for μ-PIV only a local stream-tube seeding is appropriate. In case of a global seeding, absorption and multiple particle scattering reduce the image quality.
5. Systematic measurement errors caused by the high intensity at the focal-line of the incident light sheet were measured and quantified. The maximum displacement was 0.5 pixels (0.45 μm) after 20 μs. This implies that the resulting measurement uncertainty is negligible.
6. Determination of the wall-shear-stress at 5 Reynolds numbers indicates a clear linear relationship between the shear-stress and the Reynolds number (Table 1).
7. Excellent agreement with the theory in the viscous sub-layer and the buffer-layer (Fig. 9).
8. Logarithmic law fitted to the reference measurement yields $\kappa = 0.35$ and $B = 4.98$, close to recently determined $\kappa = 0.35$ by Österlund et al. (2000).
9. Power law fitted to the reference measurement yields $C = 8.37$ and $n = 0.17$.
10. The fit of the two laws to the data is equally good, which implies that measurements over a larger Reynolds numbers range are necessary in order to properly evaluate these laws.
11. RMS fluctuations also show a good correspondence to existing experimental data. It seems, based on the measurements with a higher spatial resolution, that the wall parallel velocity fluctuation does not reach the value 3 in normalised units (Fig. 10).

**Final conclusion:** To validate the fluid mechanical question whether or not the constants $\kappa$ and $B$ are really dependent on the Reynolds number, further experiments over a larger Reynolds number range are required. They should be performed in a high quality flow facility which is especially designed for boundary layer investigations. However, the digital large format long distance μ-PIV technique developed and examined in this contribution is now well qualified for such investigations. In addition, this technique can be applied for the examination of technical flows in medium sized wind-tunnels (up to 1350 mm observation distance).

## 7
## References

**Adrian RJ** (1997) Dynamic ranges of velocity and spatial resolution of particle image velocimetry. Meas. Sci. Technol., 8, pp. 1393-1398

**Adrian RJ** (1988) Statistical properties of particle image velocimetry measurements in turbulent flow. In Laser Anemometry in Fluid Mechanics III, Springer-Verlag, Berlin Heidelberg, pp. 115–129

**Barenblatt GI** (1993) Scaling Laws for Fully Developed Turbulent Shear Flows, Parts 1 & 2. J. Fluid Mech., Vol. 248, pp. 513–529

**Bergmann L; Schäfer C** (2004) Lehrbuch der Experimentalphysik Bd. 3 Optik, de Gruyter, Berlin New York

**Billy F; David L; Pineau G** (2004) Single pixel resolution correlation applied to unsteady flow measurements. Meas. Sci. Technol. Vol 15, pp. 1039–1045

**Clauser FH** (1954) Turbulent boundary layers in adverse pressure gradients. J. Aeronaut. Sci., Vol. 21, pp. 91–108

**Dieterle L** (1997) Entwicklung eines abbildenden Meßverfahrens (PIV) zur Untersuchung von Mikrostrukturen in turbulenten Strömungen. PhD thesis, Deutscher Universitätsverlag, Wiesbaden, Germany

**Fernholz HH; Finley PJ** (1996) The incompressible zero-pressure-gradient turbulent boundary layer: An assessment of the data, Prog. Aerospace Sci. Vol. 32, pp. 245–311

**Infinity:** http://www.infinity-usa.com/Products/pro_Model_K2.aspx

**Kähler CJ** (2003) General design and operating rules for seeding atomisers. Proc. of the 5th Int. Symp. on Particle Image Velocimety, Busan, Korea, Sept. 22–24

**Kähler CJ** (2004) The significance of coherent flow structures for the turbulent mixing in wall-bounded flows. Dissertation der Georg-August-Universität zu Göttingen. http://webdoc.sub.gwdg.de/diss/2004/kaehler/kaehler.pdf

**Kähler CJ** (2004b) Investigation of the spatio-temporal flow structure in the buffer region of a turbulent boundary layer by means of multiplane stereo PIV. Exp. Fluids **36**, pp. 114–130

**Kähler CJ; Dreyer M** (2004) Dynamic 3D stereoscopic PIV and Schlieren investigation of turbulent flow structures generated by laser induced plasma. Proc. of the 12th Int. Symp. on Appl. of Laser Techn. to Fluid Mech. Lisbon, Portugal, July 12–15, paper 16–6

**Kähler CJ; Sammler B; Kompenhans J** (2002) Generation and control of particle size distributions for optical velocity measurement techniques in fluid mechanics. Exp. Fluids 33, pp. 736–742

**Kähler CJ; Scholz U** (2003) Investigation of laser-induced flow structures with time-resolved PIV, BOS and IR technology. Proc. of the 5th Int. Symp. on Particle Image Velocimety, Busan, Korea, Sept. 22–24

**Lindken R; Di Silvestro F; Westerweel J; Nieuwstadt FTM** (2002) Turbulence measurements with µ-PIV in large-scale pipe flows. Proc. of the 11th Int. Symp. on Appl. of Laser Techn. to Fluid Mech. Lisbon, Portugal, July 8–11, paper 12–1

**Meinhart CD; Wereley ST; Santiago JG** (2000) Micron resolution velocimetry techniques. In: Laser techniques applied to fluid Mechanics: Selected papers from the 9th Int. Symp. on Appl. of Laser Techn. to Fluid Mech., Lisbon, Springer, Berlin, Germany, pp. 57–70

**Österlund JM; Johansson AV; Nagib HM; Hites MH** (2000) A Note on the Overlap Region in Turbulent Boundary Layers. Phys. Fluids, 12 (1), pp. 1–4

**Questar:** http://www.company7.com/questar/microscope.html

**von Kármán T** (1930) Mechanische Ähnlichkeit und Turbulenz. Nachrichten v. d. Gesellschaft der Wissenschaften zu Göttingen Math. Phys. Klasse, pp. 58–76

**Wereley ST; Meinhart CD; Gray HB** (1999) Depth effects in volume illuminated PIV. Proc. of the 3th Int. Symp. on Particle Image Velocimety, Santa Barbara, CA, USA, Sept. 16–18

**Westerweel J; Geelhoed P; Lindken R** (2004) Single-pixel resolution ensemble correlation for micro-PIV applications. Exp. Fluids, Vol. 37, pp. 375–384

**Winter KG** (1977) An outline of the techniques available for the measurement of skin friction in turbulent boundary layers. Prog. Aerospace Sci., Vol. 18, pp. 1–57

**Zagarola MV; Smith AJ** (1997) Scaling of the mean velocity profile for turbulent pipe flow. Phys. Rev. Lett. 78 (2), pp. 239–242

**Zanoun ES; Durst F; Nagib H** (2003) Evaluating the law-of-the-wall in 2D fully developed turbulent channel flow. Phys. Fluids, Vol. 15, pp. 3079–3089